Quasi-Casimir coupling induced phonon heat transfer across a vacuum gap

Wentao Chen[a], Gyoko Nagayama[b,*]

[a] *Graduate School of Engineering, Kyushu Institute of Technology, 1-1 Sensui, Tobata, Kitakyushu, Fukuoka 804-8550, Japan*

[b] *Department of Mechanical Engineering, Kyushu Institute of Technology, 1-1 Sensui, Tobata, Kitakyushu, Fukuoka 804-8550, Japan*

* Corresponding author.

E-mail address: nagayama.gyoko725@mail.kyutech.jp (G. Nagayama).

ABSTRACT

In vacuum, thermal energy is transported by photons (thermal radiation) but not phonons. Recent studies, however, indicated that phonon heat transfer across a vacuum gap is mediated by the quantum fluctuation of electromagnetic fields. Specifically, in the heat exchange between two objects separated by a nanoscale vacuum gap, phonons carry thermal energy more efficiently than photons. However, it remains unclear if phonons can propagate without electromagnetic fields. Here, we demonstrate that phonon transmission across a sub-nanometer vacuum gap can be induced by quasi-Casimir force subjected to the Lennard–Jones atoms using classical molecular dynamics simulation. The net heat flux across the vacuum gap increases exponentially as the gap distance decreases, owing to acoustic phonon transmission. The local heat flux, evaluated using the Irving–Kirkwood method, increases singularly at the interfacial layers, while that at the inner layers agrees well with the net heat flux. These findings provide evidence of the strong thermal resonance induced by quasi-Casimir coupling between the interfacial layers. Thus, we conclude that the quasi-Casimir coupling induced by intermolecular interaction is a heat transfer mode for phonon heat transfer across a vacuum gap in nanoscale.

Keywords: Quasi-Casimir coupling; Thermal resonance at interface; Phonon transmission; Near field heat transfer; Nanoscale vacuum gap; Molecular dynamics simulation

Nomenclature

a	lattice constant of platinum, m
A	cross-sectional area of the xy-plane, m^2
D	vacuum gap distance, m
E_C	cumulative output energy, J
E_H	cumulative input energy, J
E_i^k	kinetic energy of molecule i, J
F_{ij}	intermolecular force between pair molecules i and j, N
G	thermal conductance, W m^{-2} K^{-1}
J_{is}	local heat flux corresponding to self-wall molecular interaction, W m^{-2}
J_{io}	local heat flux corresponding to other wall molecular interaction, W m^{-2}
J_k	local heat flux corresponding to molecular kinetic energy, W m^{-2}
J_p	local heat flux corresponding to molecular potential energy, W m^{-2}
J_q	local heat flux, W m^{-2}
k_B	Boltzmann constant, m^2 kg s^{-2} K^{-1}
L_x	length of simulation cell in x-direction, m
L_y	length of simulation cell in y-direction, m
L_z	length of simulation cell in z-direction, m
m	mass of an atom, kg
N	number of atoms
q	heat flux, W m^{-2}
r_{ij}	distance between pair molecules i and j, m
t_f	long finite time, s
t_0	initial time, s
ΔT	temperature difference between two thermostats, K
T	local temperature of each bin, K
T_{Ci}	temperature of interfacial layer at cooling wall, K
T_{Hi}	temperature of interfacial layer at heating wall, K
$\bar{v}_i$	mean velocity component i (=x, y, z), m s^{-1}
v_j	velocity of molecule j, m s^{-1}
$v_{n,i}$	velocity component i (=x, y, z) of atom n, m s^{-1}

$v_{z,i}$ velocity component of molecule *i* in z-direction, m s^{-1}

$\Delta z_{i,t}$ vibrational displacement of atom *i* at time *t*, m

$\bar{z}$ equilibrium position of an atom in z-direction, m

$z_{i,t}$ z position of atom *i* at time *t*, m

Greek symbols

ε energy parameter of potential function, J

ϕ pair potential, J

σ length parameter of potential function, m

ω angular frequency, rad/s

Subscripts

C cooling wall

H heating wall

i interface

x x-direction

y y-direction

z z-direction

1. Introduction

Nanoscale heat transfer has been a challenging research topic since last decade [1–36]. The scale of the gap distance D dominates the heat transfer between two objects at different temperatures in vacuum, from the conventional heat conduction ($D = 0$) to thermal radiation ($D > \lambda_T$, Wien's wavelength $\lambda_T \cong 10^{-5}$ m at room temperature) [1]. As shown in Fig. 1, when the objects are separated by a gap of $D < \lambda_T$, known as the regime of the near-field radiative heat transfer (NFRHT), the amount of heat transfer can be several orders of magnitude greater than Planck's blackbody limit [2–7]. Therefore, the NFRHT has attracted considerable interest in advanced applications of thermal management [8,9], radiative cooling [10,11], nanogap near-field thermophotovoltaics [12], and heat-assisted magnetic recording [13,14].

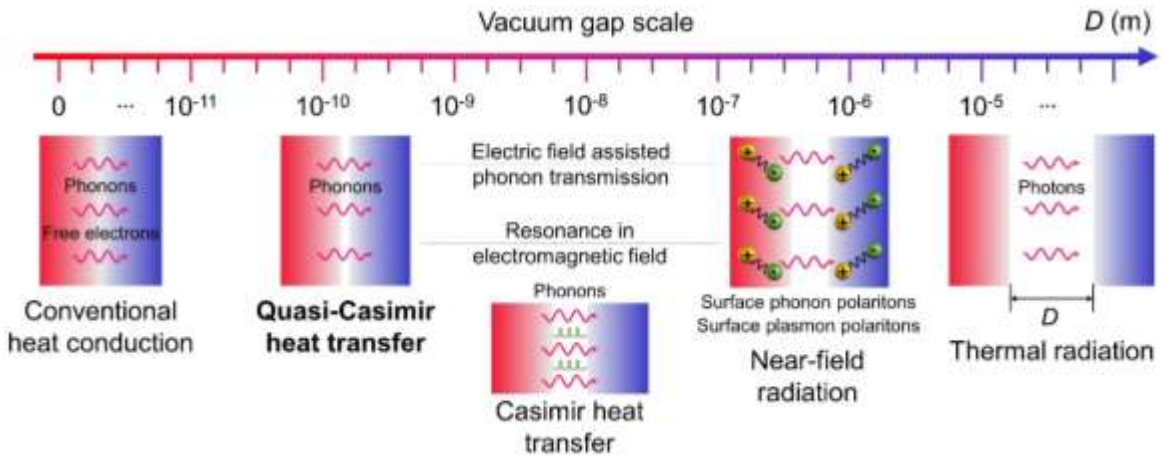

Fig. 1. Scale of a vacuum gap dominates the heat transfer mechanism between two objects.

The thermal energy transported by the coupling between the electromagnetic waves of the heating object and the phonons or plasmons of the cooling object in the regime of NFRHT, has been explored using the fluctuating electrodynamics theory [15] and experiments [16–18]. In the regime of $D < 10^{-7}$ m, the atomic Coulomb interaction between two polar nanoparticles dominates the NFRHT in the gap distance of 8–100 nm [19], while the phonons serve as effective thermal carriers between two objects separated by a nanometer vacuum gap [20–28]. In particular, phonon coupling in electric fields becomes significant in the transition regime from NFRHT to heat conduction. The existence of an extra tunnel for thermal energy transfer across a gap of 0–2.8 nm between two NaCl slabs was proposed due to phonon coupling induced by long-range Coulomb forces in the electric fields [29]. The acoustic phonons theoretically dominate the heat transfer across a gap of 1–5 nm between two Au surfaces applied a bias voltage of 0.6 V [30]. Furthermore, acoustic phonon transport has been experimentally observed in gaps ranging from 0–10 nm between a silicon tip and a platinum nano-heater under a bias voltage of 0.8 V [31]. However, clarifying the mechanism of the electric field assisted phonon transmission across a vacumm gap in this transition regime is still a challenging work.

On the other hand, Casimir heat transfer induced by resonance in electromagnetic fields was proposed in the transition regime from NFRHT to heat conduction. The Casimir force was first introduced in 1948 as a force acting between neutral objects based on quantum fluctuations of electromagnetic fields [32]. A local model of the dielectric function was applied to explain the phonon coupling mechanism induced by the Casimir force across a vacuum gap of $D < 10$ nm

between two dielectric solids [33]. The quantum fluctuation has been found to resonantly enhance the heat exchange between two Si_3N_4 membranes at $D < 400$ nm in an electromagnetic field [34].

However, the phonon heat transfer due to the thermal resonance induced by quasi-Casimir coupling has never been verified without an electromagnetic field. To this end, in this study, a quasi-Casimir coupling model is proposed for phonon heat transfer between two parallel solid walls separated by a sub-nanometer vacuum gap in the absence of an electromagnetic field. The phonon heat transfer is investigated in systems by performing a classical molecular dynamics (MD) simulation to verify the quasi-Casimir coupling model. Consequently, we evidence the phonon heat transfer induced by the intermolecular interactive force across the vacuum gap with significant interfacial resonance.

2. Models and simulation method

2.1. Physical model

Consider two solid walls that consist of monoatomic molecules connected by springs, which correspond to the harmonic potential at heating and cooling walls, as illustrated in Fig. 2(a). The two solid walls are bonded with a quasi-Casimir coupling characterized by the spring coupling in a vacuum gap. This quasi-Casimir coupling acts as the channel for phonon transmission in the vacuum gap, which is similar to acoustic phonon tunneling in an evanescent electric field, thus providing an additional channel to enhance thermal energy transfer across the vacuum gap [29]. A constant heat flux q passes through the vacuum gap with thermal conductance G from the interfacial layer of the heating wall at a high temperature T_{Hi} to that of the cooling wall at a low temperature T_{Ci}.

2.2. MD simulation method

The MD technique [37–40] was applied to simulate thermal energy transport across the sub-nanometer vacuum gap between the heating wall (red wall heated by a thermostat layer of 120–300 K) and the cooling wall (blue wall cooled by a thermostat layer of 100 K). The velocity scaling method was used to maintain the temperatures of the heating and cooling thermostats [41]. The two parallel solid walls were separated by a gap distance D of 0–0.784 nm (0–2a), where a denotes the lattice constant of platinum and is equivalent to 0.392 nm [42], as shown in Fig. 2(b). As D decreases, the strength of the intermolecular interactions between two solid walls in vacuum

increases, which induces the quasi-Casimir coupling with high thermal energy transport, as will be described in Section 3.

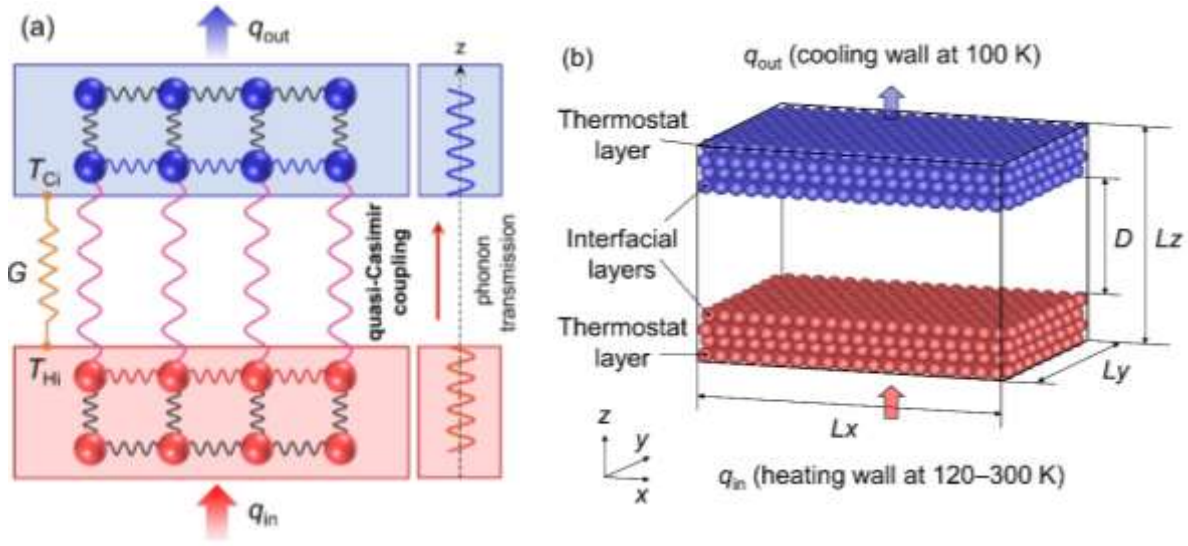

Fig. 2. (a) Schematic of acoustic phonon transmission across a vacuum gap by quasi-Casimir coupling. (b) MD simulation system: heat exchange between two parallel solid walls separated by a gap distance *D*.

The dimensions of the simulation cell are *Lx* = 5.552 nm, *Ly* = 3.847 nm, and *Lz* = 1.813–2.597 nm. Each solid wall consists of four layers of atoms that are settled as <111>-oriented face-centered cubic lattices. The solid walls are presumed to be composed of 2,560 platinum atoms. Periodic boundary conditions are employed along the x- and y-directions. The solid–solid interaction is expressed by the Lennard–Jones potential as follows:

$$\phi\left(r_{ij}\right)=4\varepsilon\left[\left(\frac{\sigma}{r_{ij}}\right)^{12}-\left(\frac{\sigma}{r_{ij}}\right)^{6}\right], \tag{1}$$

where the length parameter σ = 2.475 Å and the energy parameter $\varepsilon = 8.35\times10^{-20}$ J for the potential well depth of Pt–Pt to model the atomic vibration at the lattice. All of the simulations are implemented with a time step of 5 fs and a cut-off radius of 5σ selected for the spherically truncated and shifted potential. The equations of motion are integrated using the velocity Verlet algorithm.

The equilibrium system at 100 K is simulated after achieving a steady state from the initial state for 5 ns. Subsequently, the non-equilibrium molecular dynamics (NEMD) simulation is performed from the equilibrium state to the steady state for 50 ns. In all of the NEMD simulations, the

cumulative input and output energies E_H and E_C in the heating (120–300 K) and cooling (100 K) thermostats, respectively, are monitored. After the system achieves a steady state with constant heat flow ($\Delta E \cong 0$), an extra un-steady NEMD simulation is conducted by switching off the cooling thermostat but operating the heating thermostat for 5 ns. The transient thermal behaviors are discussed in Section 3.1. Further data analyses for the steady NEMD simulations are described in the next section.

2.3. Computational details

The simulation system is divided into eight bins along both the x- and z-directions to obtain the temperature profile in the steady state for 5 ns. The local temperature T of each bin can be calculated as follows:

$$T = \frac{1}{N}\sum_{n=1}^{N}\frac{2}{3k_B}\sum_{i=1}^{3}\frac{1}{2}m\left(v_{n,i}-\overline{v}_i\right)^2, \tag{2}$$

where N is the particle number in the bin, k_B is the Boltzmann constant, m is the mass of the solid atom, $v_{n,i}$ is the velocity of atom n in the i (=x, y, z) direction, and $\overline{v}_i$ is the mean velocity of the solid atoms in the bin.

The heat flux passing through the system is acquired from the mean value over the last 15 ns within a 50 ns time window. The heat flux is

$$q = \frac{1}{A}\cdot\frac{\partial E}{\partial t}, \tag{3}$$

where A is the cross-sectional area of the xy-plane, $\partial E / \partial t$ is the rate of heat transfer in the heating or cooling thermostat, and E is the cumulative energy of the heating (E_H) or cooling (E_C) thermostat. The thermal conductance between the two solid walls is calculated as

$$G = \frac{q}{T_{Hi} - T_{Ci}}. \tag{4}$$

The atomic vibrational displacements and frequencies are measured using a wave graph to observe the vibrational properties of the atoms at the positions (A2, A3, A4 and B2, B3, B4) shown in Fig. 3. The wave graphs are obtained by outputting the positions of the atoms from the MD simulation data of 10,000 time steps and conducting signal processing [43]. The equilibrium position of the atoms in the z-direction is calculated by:

$$\overline{z} = \frac{1}{t_f - t_0}\sum_{t_0}^{t_f} z_{i,t}, \tag{5}$$

where $z_{i,t}$ is the position of atom i at time t, and atom i is located at the center of each solid layer; t_0 is the initial time at which the data output begins, and t_f is the long finite time for 10,000 time steps. The original vibrational displacements of atom i are calculated as $\Delta z_{i,t} = z_{i,t} - \bar{z}$. Then, we calculate the Fourier transform of the original vibrational displacements to obtain the distribution of signal power in the frequency domain (power spectrum). The dominant frequency band is selected to perform signal filtering on the original vibrational displacements and obtain the regular wave graphs. The peak amplitude and frequency are determined from the wave graphs.

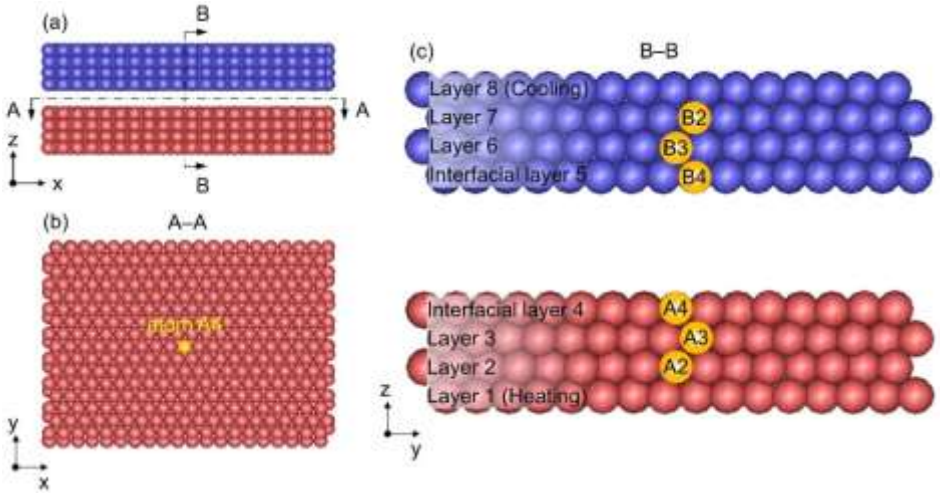

Fig. 3. Positions of atoms selected to analyze the atomic vibrational characteristics from different views of the simulation model: (a) front view of the simulation model in the xz-direction; (b) atom A4 at interfacial layer 4 in the A–A directional view of the simulation model; (c) atoms A2, A3, A4 and B2, B3, B4 of the solid layers in the B–B directional enlarged view of the simulation model.

The velocities of all the atoms in the interfacial layers obtained from the MD simulation data of 10,000 time steps, are used to calculate the vibrational density of states (VDOS) [44,45] of the interfacial layers by the Fourier transform of the velocity autocorrelation function

$$VDOS(\omega) = \int_0^\infty \left\langle \vec{v}(t)\vec{v}(0) \right\rangle e^{-i\omega t} dt . \quad (6)$$

Here, ω is the angular frequency, and $v(t)$ is the atomic velocity at time t.

The simulation system is divided into eight bins along both the x- and z-directions to calculate the average local heat flux of each layer. The components of thermal energy are calculated to

estimate the effective energy of heat transfer across a vacuum gap along the z-direction by using the Irving–Kirkwood (I–K) equation [46, 47],

$$J_q = J_k + J_p + J_i = \frac{1}{V}\sum_i E_i^k v_{z,i} + \frac{1}{V}\sum_i \phi_i v_{z,i} + \frac{1}{2V}\sum_i \sum_j \left(F_{ij} v_j\right) r_{z,ij} \,, \tag{7}$$

where J_k and J_p represent the energies transported by the molecules with kinetic and potential energy, respectively, and J_i represents the intermolecular energy transfer. V is the volume of the solid layer, E_i^k is the kinetic energy of molecule i, ϕ_i is the potential energy of molecule i, $v_{z,i}$ is the velocity component of molecule i along the z-direction, F_{ij} is the intermolecular force between molecules i and j, v_j is the velocity of molecule j, and $r_{z,ij}$ is the distance between molecules i and j along the z-direction.

3. Results and discussion

3.1. Transient thermal behavior in non-steady state

Since the temperature differences between the heating and cooling walls in the steady NEMD simulations can be maintained if the vacuum gap acts as the thermal insulation, we conducted the non-steady NEMD simulations to confirm if thermal energy can be transported from the heating wall to the cooling wall across the vacuum gap. The transient thermal behavior of the system is investigated based on the time history of the temperatures at the interfacial layers. The temperatures shown in Fig. 4 are obtained in the non-steady NEMD simulations by operating the heating thermostat but switching off the cooling thermostat. The temperature difference between the interfacial layers of the heating and cooling walls separated by $D = 0.5a$ is eliminated after a certain period of time within 5 ns, thus demonstrating the occurrence of thermalization between the two solid walls. This phenomenon indicates that energy must be transferred from the heating wall to the cooling wall across a vacuum gap, even for the Lennard–Jones atoms, in the absence of an electromagnetic field. The heat transfer between the two walls is enhanced with an increment in the temperature difference between thermostats ΔT at $D = 0.5a$, as shown in Figs. 4(a)–(c); while diminishes with an increase in D at $\Delta T = 100$ K as shown in Figs. 4(c)–(e), owing to the weakened interaction between the two interfacial layers.

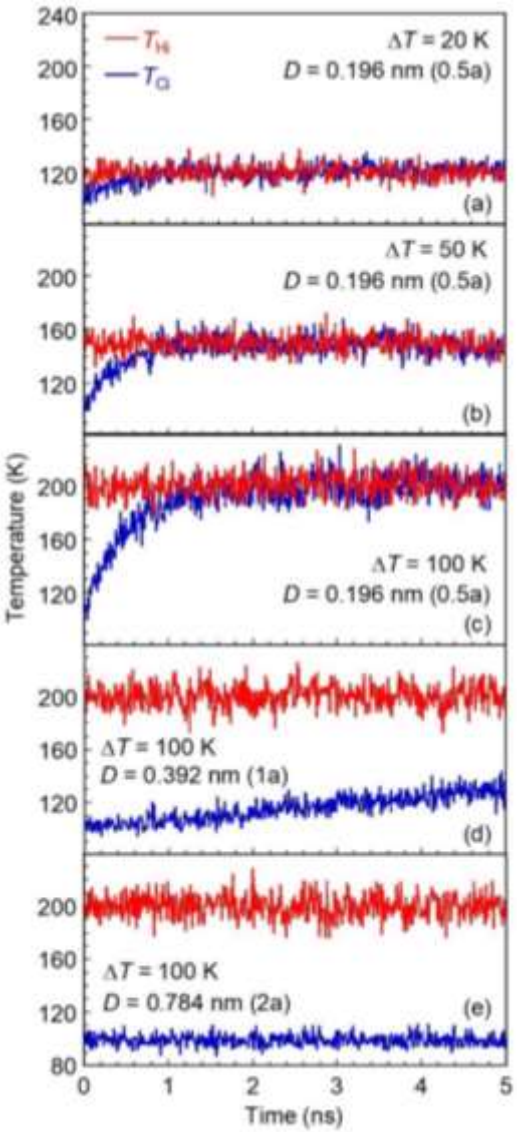

Fig. 4. Thermal energy transport across a vacuum gap in non-steady NEMD simulations: (a–c) effects of ΔT on the transient temperature of the interfacial layers at constant $D = 0.5a$; (c–e) effects of D on the transient temperature of the interfacial layers at constant $\Delta T = 100$ K.

3.2. Temperature profiles in steady state

The temperature profiles shown in Fig. 5 are obtained under the operation of the simultaneous heating and cooling thermostats after the NEMD system achieves a steady state, where the solid lines are guide for the eye. Figs. 5(a)–(e) are results under the constant temperature difference between the two thermostats ($\Delta T = 20$ K). In the case of $D = 0$, as shown in Fig. 5(a), a continuum temperature distribution is obtained from the cooling thermostat to the thermostat free layers, while

a temperature jump is found between the heating thermostat and the neighboring thermostat free layer. This temperature jump is caused by the phonon mismatch between the thermostat and thermostat free layer owing to the dynamic rescaling of the thermostat [48,49]. Increasing D from 0.5a to 2a (ΔT = 20 K), as shown in Figs. 5(b)–(e), the temperature distributes continuously in the inner layers, while discontinuously at the interfacial layers. The temperature jump at the interfacial layers (T_{Hi} - T_{Ci}) is nearly identical to ΔT and independent of the gap distance D. In the case of D = 0.5a, as shown in Fig. 5(f), the temperature gradient of heating wall is nearly same as that of cooling wall, and T_{Hi} - T_{Ci} gets larger with an increment in ΔT, showing the enhanced thermal energy exchange between the two solid walls.

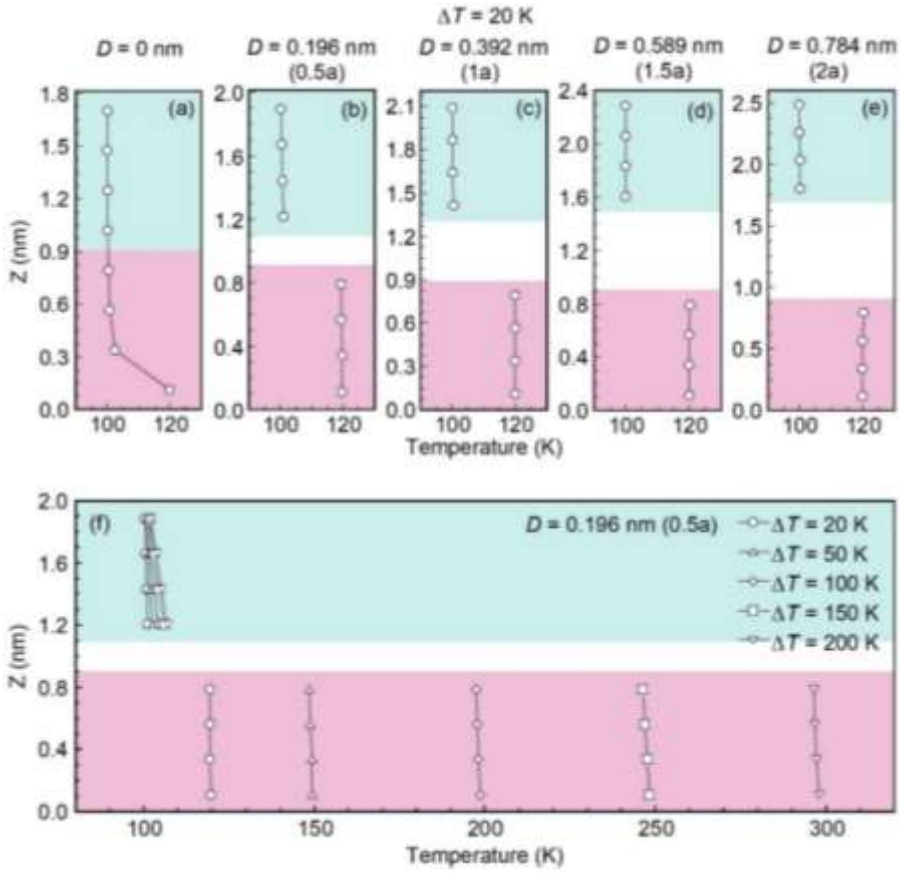

Fig. 5. Temperature profiles of the solid walls in steady NEMD simulations: (a–e) varying D at constant ΔT = 20 K; (f) varying ΔT at constant D = 0.196 nm (0.5a).

3.3. Net heat flux and thermal conductance

In the steady state of the NEMD simulation, the net heat flux and thermal conductance are obtained by conducting data sampling over a period of 15 ns. The net heat flux and thermal

conductance in the sub-nanometer gap are approximately three to six orders of magnitude larger than that of blackbody radiation as a function of D, as shown in Figs. 6(a) and (b). These results give evidence of the existence of another heat transfer mode between the regimes of thermal radiation and heat conduction. This exponential heat transfer enhancement occurs owing to the strengthened intermolecular interaction between the two solid walls as D decreases. The heat flux and thermal conductance in the case of $D = 0$ are larger than those for other cases of D due to the heat conduction in solid objects. Furthermore, the heat flux enhances with an increment in ΔT, while ΔT does not notably influence the thermal conductance, as shown in Figs. 6(c) and (d).

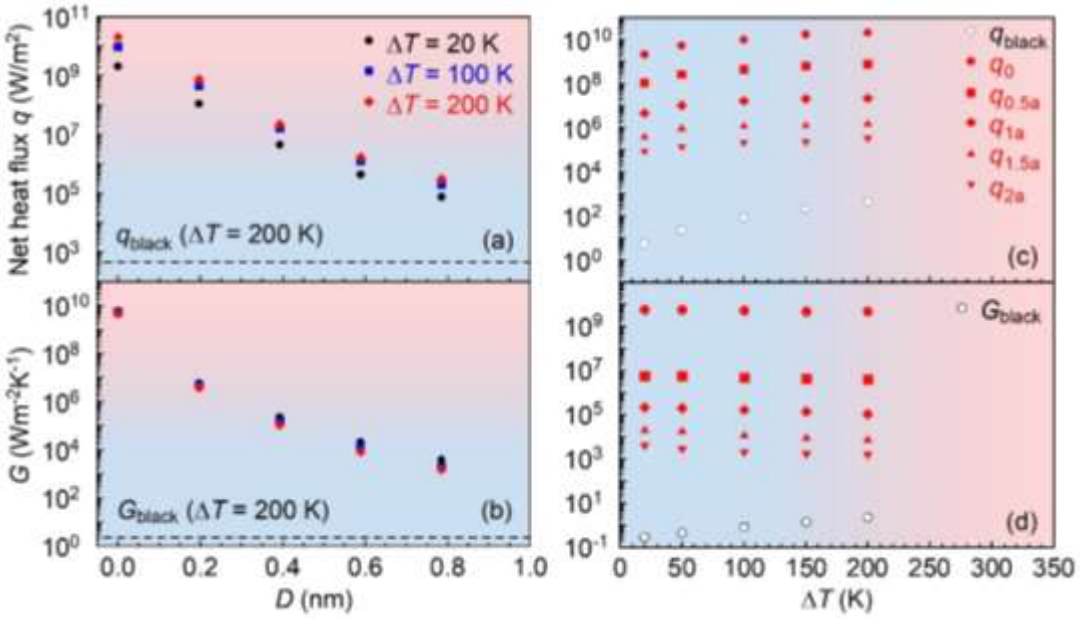

Fig. 6. Effects of D on (a) net heat flux and (b) thermal conductance. Effects of ΔT on (c) net heat flux and (d) thermal conductance.

3.4. Thermal resonance induced by quasi-Casimir coupling

To understand the mechanism of heat transfer enhancement with decreasing D, as shown in Fig. 6, we analyzed the atomic vibrational characteristics in a steady NEMD state under a constant ΔT of 20 K. For $D = 0.5a$, the peak amplitudes of the interfacial atoms (A4 at the heating wall, B4 at the cooling wall) are significantly larger than those of the atoms (A2, A3, B2, B3) in the inner layers, as shown in Figs. 7 (b) and (e) and summarized in Table 1. Meanwhile, the vibrational frequencies of the interfacial atoms (A4, B4) are smaller than those of the inner layer atoms, as listed in Table 1. These deviations are unremarkable when $D = 2a$, as shown in Figs. 7(c) and (f),

while the peak amplitudes and frequencies of the inner layer atoms at $D = 0$ are similar, as shown in Figs. 7(a) and (d). That is, when D is sufficiently small (several atomic diameters), the interfacial atoms are subjected to strong molecular interactions across the vacuum gap, which results in the thermal resonance induced by quasi-Casimir coupling. This aspect can be proved by the perfectly overlapped vibrational displacements of the interfacial atoms A4 and B4 separated by the vacuum gap in Figs. 8(b) and (c), which show vibration behaviors similar to those of the inner layer atoms in the solid wall shown in Fig. 8(a). Therefore, the VDOSs based on the Fourier transform of the atomic velocity autocorrelation function [44,45] of solid layer 4 are consistent with those of layer 5, as shown in Figs. 8(d)–(f). Compared to the peaks of the VDOSs of the inner layers in the solid ($D = 0$), those of the interfacial layers ($D = 0.5a$ or $2a$) are shifted toward the left of the low-frequency band. That is, the heat transfer across the sub-nanometer vacuum gap between the solid walls exhibits a trend similar to that of the solid walls without a gap, conducted through the acoustic phonons in the low-frequency band of 3–4 THz. The strong phonon coupling at the interfacial layers leads to the resonant excitation peaks of the VDOSs in the frequency band coinciding with the vibrational frequencies of the interfacial atoms A4 and B4, as summarized in Table 1. These results indicate that the gap distance D is the dominant factor governing the near-field heat transfer induced by the quasi-Casimir coupling.

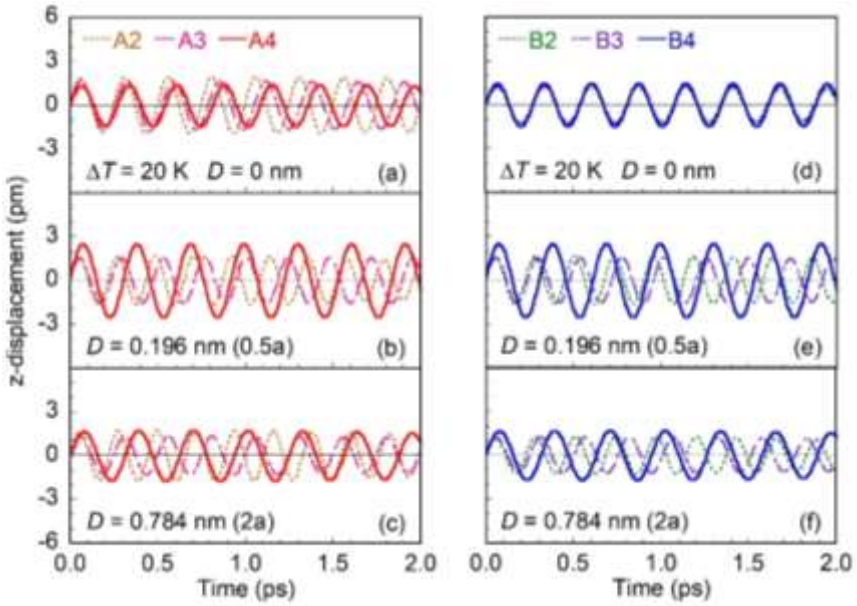

Fig. 7. Effects of D on atomic vibrational displacements of layers in the heating and cooling walls at constant ΔT = 20 K: (a–c) vibrational displacements of atoms A2, A3, and A4 in the heating wall; (d–f) vibrational displacements of atoms B2, B3, and B4 in the cooling wall.

Table 1

Effects of D on the peak amplitudes and frequencies of atoms in the interfacial and inner layers at constant ΔT = 20 K.

Cases / D (nm)	A2	B2	A3	B3	A4	B4
Peak amplitude (pm)						
0	1.909	1.244	1.722	1.246	1.471	1.468
0.196	1.646	1.583	1.570	1.559	2.775	2.526
0.784	1.733	1.302	1.335	1.235	1.734	1.693
Frequency f (THz)						
0	4.041	3.699	3.790	3.701	3.736	3.727
0.196	4.578	4.452	4.207	4.207	3.277	3.257
0.784	4.483	4.359	4.017	3.949	3.180	3.149

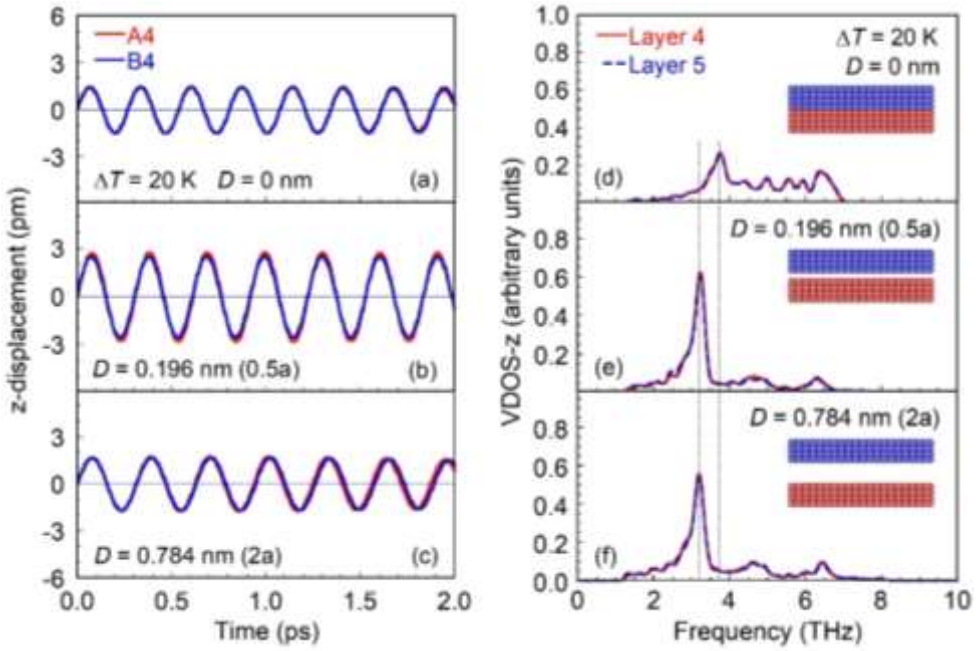

Fig. 8. Effects of *D* on (a–c) the vibrational displacements of atoms A4 and B4 in the interfacial layers as well as (d–f) the VDOSs of layers 4 and 5.

3.5. Local heat flux

For the estimation of the local thermal properties in the heat exchange between two solid walls from an atomic perspective, a stable local heat flux distribution is established through data sampling for more than 50 ns by using the I-K method [46,47], as shown in Fig. 9. The blue dashed lines represent the net heat flux of the system obtained from the energy balance of the two thermostats, the open circles are the local heat flux of each layer, and the black solid lines are guide for the eye. The component contributions of the heat transfer enhancement induced by the quasi-Casimir coupling are analyzed, as shown in Fig. 10. The local heat flux J_q of each solid layer is composed of four components, namely J_k, J_p, J_{is}, and J_{io} corresponding to the kinetic energy, potential energy, self-wall molecular interaction, and other wall molecular interaction, respectively.

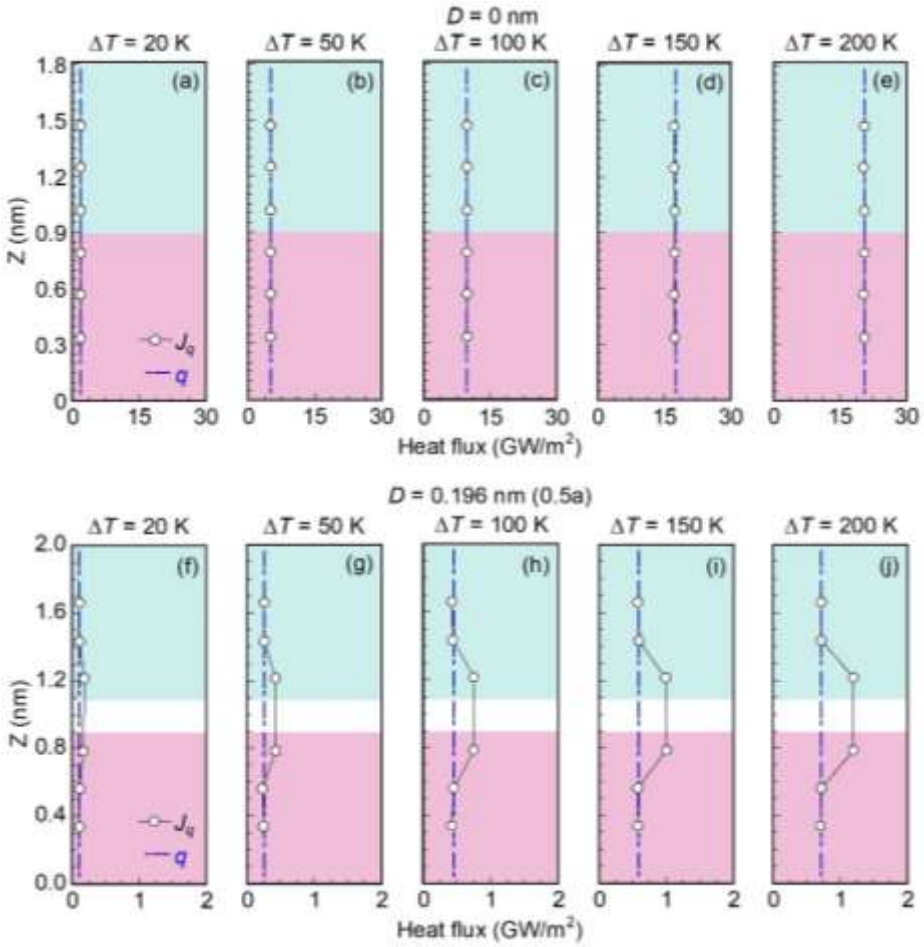

Fig. 9. Effects of ΔT on the local heat flux of the interfacial and inner layers along the z-direction at (a–e) $D = 0$ and (f–j) $D = 0.5a$.

When $D = 0$, J_q is distributed uniformly and gets larger as ΔT increases, as shown in Figs. 9(a)–(e). J_q satisfies the energy conservation law, which is equivalent to the net heat flux q obtained from the energy balance of the two thermostats. Clearly, the local heat flux components J_{is} and J_{io} dominate the thermal energy transport in the solid, and J_k and J_p are negligible, as shown in Figs. 10(a)–(c). Here, J_{is} and J_{io} contribute equally at inner layers 4 and 5. When $D = 0.5a$ (i.e., interfacial quasi-Casimir coupling), the local heat flux increases singularly at the interfacial layers, whereas it is distributed uniformly at the inner layers, corresponding to q, as shown in Figs. 9(f)–(j). The local heat flux at the interfacial layers enhances singularly, accompanied by considerable thermal resonance induced by quasi-Casimir coupling (see Figs. 7(b) and (e)). In Fig. 10(d)–(f), the singular increments of the local heat flux at the interfacial layers are contributed to the increments of J_{io} (orange) and J_p (blue). Although J_{is} (green) is almost same to the half of q, J_{io} exceeds the

half of q, owing to the thermal resonance induced by the quasi-Casimir coupling. Additionally, the interfacial vibration energy increases under the thermal resonance, resulting in the increment of J_p at the interface. In other words, the singular increments of the local heat flux at the interfacial layers can be regarded as the evidence of the quasi-Casimir coupling.

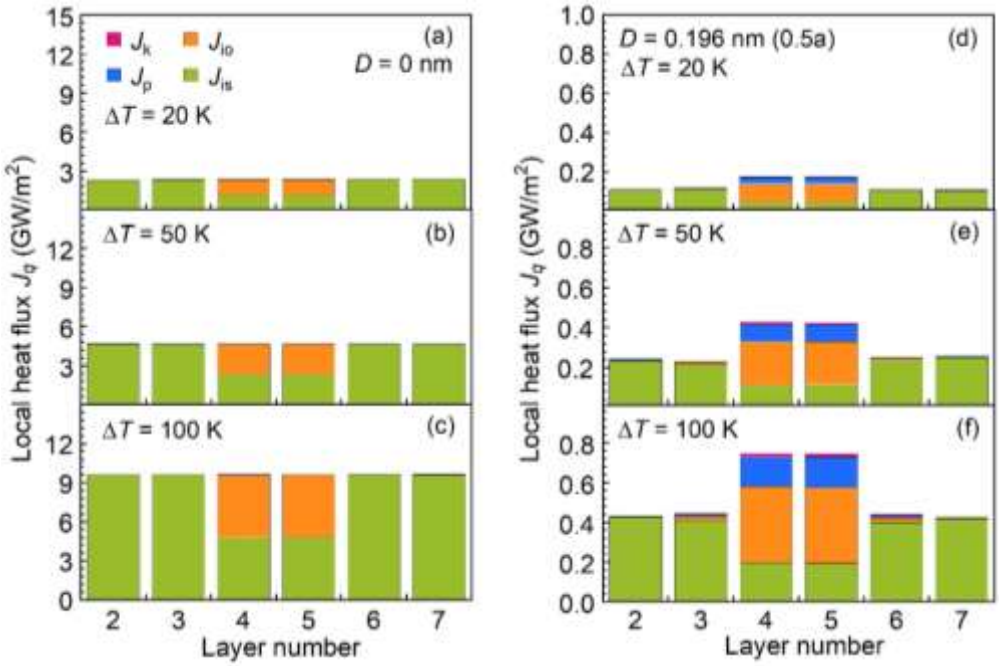

Fig. 10. Effects of ΔT on the contributions of the thermal energy components to the local heat flux at the interfacial and inner layers at (a–c) $D = 0$ and (d–f) $D = 0.5a$.

4. Conclusion

MD simulations were performed to investigate the phonon heat transfer across a vacuum gap induced by the quasi-Casimir force subjected to the Lennard–Jones atoms. We demonstrated that the heat exchange between two solid walls separated by a sub-nanometer vacuum gap increases exponentially as the gap distance decreases, following the law of energy conservation. The heat transfer enhancement is caused by the acoustic phonon transport across a vacuum gap, as a result of the strong thermal resonance induced by the quasi-Casimir coupling. This aspect is explained by the perfect overlap of the atomic vibrational displacements and VDOSs of the interfacial layers. Moreover, the local heat flux, evaluated using the I–K method, increases singularly at the interfacial layers, while that at the inner layers is consistent with the net heat flux. This finding provides evidence of the strong thermal resonance at the two interfacial layers, induced by quasi-Casimir coupling.

The phonon transport across a vacuum gap induced by quasi-Casimir coupling, is a phenomenon independent of electrostatic interaction, electron cloud overlap, surface phonon polaritons and surface plasmon polaritons. This phenomenon is noticeably distinct from conventional heat conduction and thermal radiation, or the known NFRHT and Casimir heat transfer. The proposed quasi-Casimir coupling model of heat transfer provides fundamental insights into nanoscale energy transport between the regimes of NFRHT and heat conduction.

Declaration of Competing Interest

The authors declare that they have no known competing financial interests or personal relationships that could have appeared to influence the work reported in this paper.

CRediT authorship contribution statement

Wentao Chen: Investigation, Methodology, Data curation, Formal analysis, Writing - original draft. **Gyoko Nagayama:** Conceptualization, Methodology, Supervision, Writing - review & editing, Funding acquisition.

Acknowledgments

This work was supported by the Ministry of Education, Science and Culture of the Japanese Government through the Grant-in Aid for Scientific Research, Project No. 18H01385, the research supercomputing services by the Research Institute for Information Technology, Kyushu University, and the Initiative for Realizing Diversity in the Research Environment by Ministry of Education, Culture, Sports, Science and Technology, Japan.

References

[1] A.I. Volokitin, Contribution of the acoustic waves to near-field heat transfer, J. Phys. Condens. Matter. 32 (2020) 215001.

[2] M. Nomura, Near-field radiative heat transfer: The heat through the gap, Nat. Nanotechnol. 11 (2016) 496–497.

[3] B. Song, Y. Ganjeh, S. Sadat, D. Thompson, A. Fiorino, V. Fernández-Hurtado, J. Feist, F.J. Garcia-Vidal, J.C. Cuevas, P. Reddy, E. Meyhofer, Enhancement of near-field radiative heat transfer using polar dielectric thin films, Nat. Nanotechnol. 10 (2015) 253–258.

[4] B. Song, D. Thompson, A. Fiorino, Y. Ganjeh, P. Reddy, E. Meyhofer, Radiative heat conductances between dielectric and metallic parallel plates with nanoscale gaps, Nat. Nanotechnol. 11 (2016) 509–514.
[5] K. Kim, B. Song, V. Fernández-Hurtado, W. Lee, W. Jeong, L. Cui, D. Thompson, J. Feist, M.T.H. Reid, F.J. García-Vidal, J.C. Cuevas, E. Meyhofer, P. Reddy, Radiative heat transfer in the extreme near field, Nature 528 (2015) 387–391.
[6] M.P. Bernardi, D. Milovich, M. Francoeur, Radiative heat transfer exceeding the blackbody limit between macroscale planar surfaces separated by a nanosize vacuum gap, Nat. Commun. 7 (2016) 1–7.
[7] A. Fiorino, D. Thompson, L. Zhu, B. Song, P. Reddy, E. Meyhofer, Giant Enhancement in Radiative Heat Transfer in Sub-30 nm Gaps of Plane Parallel Surfaces, Nano Lett. 18 (2018) 3711–3715.
[8] A. Fiorino, D. Thompson, L. Zhu, R. Mittapally, S.A. Biehs, O. Bezencenet, N. El-Bondry, S. Bansropun, P. Ben-Abdallah, E. Meyhofer, P. Reddy, A Thermal Diode Based on Nanoscale Thermal Radiation, ACS Nano 12 (2018) 5174–5179.
[9] L. Zhu, A. Fiorino, D. Thompson, R. Mittapally, E. Meyhofer, P. Reddy, Near-field photonic cooling through control of the chemical potential of photons, Nature. 566 (2019) 239–244.
[10] B. Guha, C. Otey, C.B. Poitras, S. Fan, M. Lipson, Near-field radiative cooling of nanostructures, Nano Lett. 12 (2012) 4546–4550.
[11] J. Cho, K.E. Goodson, Thermal transport: Cool electronics, Nat. Mater. 14 (2015) 136–137.
[12] A. Fiorino, L. Zhu, D. Thompson, R. Mittapally, P. Reddy, E. Meyhofer, Nanogap near-field thermophotovoltaics, Nat. Nanotechnol. 13 (2018) 806–811.
[13] H. Li, B. Liu, T.C. Chong, Thermal study of nanometer-spaced head-disk systems, Jpn. J. Appl. Phys. 44 (2005) 7445–7447.
[14] E. Albisetti, D. Petti, M. Pancaldi, M. Madami, S. Tacchi, J. Curtis, W.P. King, A. Papp, G. Csaba, W. Porod, Nanopatterning reconfigurable magnetic landscapes via thermally assisted scanning probe lithography, Nat. Nanotechnol. 11 (2016) 545–551.
[15] B. V. Budaev, D.B. Bogy, Computation of radiative heat transport across a nanoscale vacuum gap, Appl. Phys. Lett. 104 (2014) 061109.

[16] L. Tranchant, S. Hamamura, J. Ordonez-Miranda, T. Yabuki, A. Vega-Flick, F. Cervantes-Alvarez, J.J. Alvarado-Gil, S. Volz, K. Miyazaki, Two-Dimensional Phonon Polariton Heat Transport, Nano Lett. 19 (2019) 6924–6930.
[17] S. Shen, A. Narayanaswamy, G. Chen, Surface phonon polaritons mediated energy transfer between nanoscale gaps, Nano Lett. 9 (2009) 2909–2913.
[18] K. Kloppstech, N. Könne, S.A. Biehs, A.W. Rodriguez, L. Worbes, D. Hellmann, A. Kittel, Giant heat transfer in the crossover regime between conduction and radiation, Nat. Commun. 8 (2017) 14475.
[19] G. Domingues, S. Volz, K. Joulain, J.J. Greffet, Heat transfer between two nanoparticles through near field interaction, Phys. Rev. Lett. 94 (2005) 085901.
[20] I. Altfeder, A.A. Voevodin, A.K. Roy, Vacuum phonon tunneling, Phys. Rev. Lett. 105 (2010) 166101.
[21] C. Yang, X. Wei, J. Sheng, H. Wu, Phonon heat transport in cavity-mediated optomechanical nanoresonators, Nat. Commun. 11 (2020) 1–6.
[22] M. Prunnila, J. Meltaus, Acoustic phonon tunneling and heat transport due to evanescent electric fields, Phys. Rev. Lett. 105 (2010) 125501.
[23] J.B. Pendry, K. Sasihithlu, R. V. Craster, Phonon-assisted heat transfer between vacuum-separated surfaces, Phys. Rev. B 94 (2016) 075414.
[24] B. V. Budaev, D.B. Bogy, On the role of acoustic waves (phonons) in equilibrium heat exchange across a vacuum gap, Appl. Phys. Lett. 99 (2011) 053109.
[25] A. Alkurdi, C. Adessi, F. Tabatabaei, S. Li, K. Termentzidis, S. Merabia, Thermal transport across nanometre gaps: Phonon transmission vs. air conduction, Int. J. Heat Mass Transf. 158 (2020) 119963.
[26] D.P. Sellan, E.S. Landry, K. Sasihithlu, A. Narayanaswamy, A.J.H. McGaughey, C.H. Amon, Phonon transport across a vacuum gap, Phys. Rev. B. 85 (2012) 024118.
[27] A.I. Volokitin, Effect of an Electric Field in the Heat Transfer between Metals in the Extreme Near Field, JETP Lett. 109 (2019) 749–754.
[28] S. Xiong, K. Yang, Y.A. Kosevich, Y. Chalopin, R. D'Agosta, P. Cortona, S. Volz, Classical to Quantum Transition of Heat Transfer between Two Silica Clusters, Phys. Rev. Lett. 112 (2014) 114301.

[29] V. Chiloyan, J. Garg, K. Esfarjani, G. Chen, Transition from near-field thermal radiation to phonon heat conduction at sub-nanometre gaps, Nat. Commun. 6 (2015) 6755.
[30] T. Tokunaga, A. Jarzembski, T. Shiga, K. Park, M. Francoeur, Extreme Near-Field Heat Transfer Between Gold Surfaces, arXiv: 2102.04575.
[31] A. Jarzembski, T. Tokunaga, J. Crossley, J. Yun, C. Shaskey, R.A. Murdick, I. Park, M. Francoeur, K. Park, Force-induced acoustic phonon transport across single-digit nanometre vacuum gaps, arXiv: 1904.09383.
[32] H.B.G. Casimir, On the attraction between two perfectly conducting plates, Proc. K. Ned. Akad. 51 (1948) 793–795.
[33] Y. Ezzahri, K. Joulain, Vacuum-induced phonon transfer between two solid dielectric materials: Illustrating the case of Casimir force coupling, Phys. Rev. B 90 (2014) 115433.
[34] K.Y. Fong, H.-K. Li, R. Zhao, S. Yang, Y. Wang, X. Zhang, Phonon heat transfer across a vacuum through quantum fluctuations, Nature 576 (2019) 243–247.
[35] M. Morita, T. Shiga, Surface phonons limit heat conduction in ultra-thin films, arXiv: 2008.11078.
[36] R. Anufriev, A. Ramiere, J. Maire, M. Nomura, Heat guiding and focusing using ballistic phonon transport in phononic nanostructures, Nat. Commun. 8 (2017) 15505.
[37] G. Nagayama, P. Cheng, Effects of interface wettability on microscale flow by molecular dynamics simulation, Int. J. Heat Mass Transf. 47 (2004) 501–513.
[38] G. Nagayama, M. Kawagoe, A. Tokunaga, T. Tsuruta, On the evaporation rate of ultra-thin liquid film at the nanostructured surface: A molecular dynamics study, Int. J. Therm. Sci. 49 (2010) 59–66.
[39] G. Nagayama, T. Tsuruta, P. Cheng, Molecular dynamics simulation on bubble formation in a nanochannel, Int. J. Heat Mass Transf. 49 (2006) 4437–4443.
[40] H. Matsubara, G. Kikugawa, T. Ohara, Comparison of molecular heat transfer mechanisms between water and ammonia in the liquid states, Int. J. Therm. Sci. 161 (2021) 106762.
[41] R.J. Sadus, Molecular Simulation of Fluids, first ed., Elsevier, Netherlands, 1999, pp. 305–307.
[42] J.W. Arblaster, Crystallographic properties of platinum, Platin. Met. Rev. 41 (1997) 12–21.
[43] A.V. Oppenheim, G.C. Verghese, Signals, Systems and Interference, first ed., Pearson, Boston, 2016, pp. 5–28.

[44] H. Bao, J. Chen, X. Gu, B. Cao, A review of Simulation Methods in Micro/Nanoscale Heat Conduction, ES Energy Environ. 1 (2018) 16–55.
[45] X. Liu, D. Surblys, Y. Kawagoe, A.R. Bin Saleman, H. Matsubara, G. Kikugawa, T. Ohara, A molecular dynamics study of thermal boundary resistance over solid interfaces with an extremely thin liquid film, Int. J. Heat Mass Transf. 147 (2020) 118949.
[46] J.H. Irving, J.G. Kirkwood, The statistical mechanical theory of transport processes. IV. The equations of hydrodynamics, J. Chem. Phys. 18 (1950) 817–829.
[47] Y. Guo, D. Surblys, Y. Kawagoe, H. Matsubara, X. Liu, T. Ohara, A molecular dynamics study on the effect of surfactant adsorption on heat transfer at a solid-liquid interface, Int. J. Heat Mass Transf. 135 (2019) 115–123.
[48] M. Barisik, A. Beskok, Boundary treatment effects on molecular dynamics simulations of interface thermal resistance, J. Comput. Phys. 231 (2012) 7881–7892.
[49] O. Yenigun, M. Barisik, Effect of nano-film thickness on thermal resistance at water/silicon interface, Int. J. Heat Mass Transf. 134 (2019) 634–640.